



HAL
open science

Automatic identification of MHD modes using Fourier transform, wavelets and computer vision algorithms

E D D Zapata-Cornejo, D Zarzoso, S D Pinches, S E Sharapov, M Fitzgerald

► **To cite this version:**

E D D Zapata-Cornejo, D Zarzoso, S D Pinches, S E Sharapov, M Fitzgerald. Automatic identification of MHD modes using Fourier transform, wavelets and computer vision algorithms. 2024. hal-04599681

HAL Id: hal-04599681

<https://hal.science/hal-04599681>

Preprint submitted on 3 Jun 2024

HAL is a multi-disciplinary open access archive for the deposit and dissemination of scientific research documents, whether they are published or not. The documents may come from teaching and research institutions in France or abroad, or from public or private research centers.

L'archive ouverte pluridisciplinaire **HAL**, est destinée au dépôt et à la diffusion de documents scientifiques de niveau recherche, publiés ou non, émanant des établissements d'enseignement et de recherche français ou étrangers, des laboratoires publics ou privés.

Automatic identification of MHD modes using Fourier transform, wavelets and computer vision algorithms

E.d.D. Zapata-Cornejo^{1,2}, D. Zarzoso¹, S.D. Pinches², S. E. Sharapov³, M. Fitzgerald³

¹ Aix-Marseille University, CNRS, Centrale Marseille, M2P2 UMR 7340, Marseille

² ITER Organization, Route de Vinon-sur-Verdon, CS 90 046, 13067 St. Paul Lez Durance Cedex, France.

³ United Kingdom Atomic Energy Authority, Culham Science Centre, Abingdon, Oxon OX14 3DB, United Kingdom of Great Britain and Northern Ireland

Abstract. MHD activity in fusion devices is typically analyzed by examining time-frequency spectrograms obtained from various diagnostics. MHD modes often co-exist with various types of noise and complex patterns generated by other events like pellet injection or active diagnostics. Traditionally, identifying MHD modes has been a manual task, making it labor-intensive. To overcome this issue, this study proposes the use of computer vision algorithms for noise removal and automatic feature extraction. First, the automatic detection of straight-line patterns is achieved by applying the Hough transform. Then, the discrete wavelet transform is proposed to break down spectrograms into sub-images of different scales, removing broadband noise and pellet injection signatures. The multiscale decomposition is subsequently extended to multiple directions using either 2D Fourier transforms or curvelets, achieving a high signal-to-noise ratio in spectrograms and eliminating undesired frequency sweeps of TAE antenna. Once MHD activity is successfully enhanced, a pipeline of algorithms for ridge detection, thresholding and labelling perform a segmentation of the image, automatically labelling individual modes. This study demonstrates the effectiveness of computer vision algorithms for the identification of MHD modes. The use of such algorithms may potentially help in the analysis process and the creation of large databases of modes.

Keywords: MHD activity, spectrograms, computer vision, wavelets, curvelets

1. Introduction

Achieving nuclear fusion requires specific plasma properties (confinement time, density and temperature) and a steady operation: free of disruptions, and instabilities. Particularly, the presence of instabilities can cause disruptions and major particle losses that can damage the plasma-facing components of magnetic fusion devices. Therefore, the detection, prevention, or control of plasma instabilities are paramount to increasing plasma performance and avoiding machine damage. Consequently, these problems are very active research topics in fusion physics and engineering.

Magnetohydrodynamic (MHD) activity, like energetic particles (EP) driven Alfvén eigenmodes [1, 2], can be observed with different diagnostic systems: magnetic sensors [3] (Mirnov coils [4]), electron cyclotron emission (ECE) [5, 6], soft X-ray measurements [7], or Far infrared interferometry (FIR) [8]. Frequently, the end product of the diagnostic analysis is a spectrogram: a time-frequency representation of the plasma oscillations.

Given magnetic fluctuations spectrograms, different finite frequency oscillations (modes) can be identified in the image. More information is needed to fully characterize these modes: radial amplitude (location), mode numbers, growth rate, and the causing drive (source of free energy). Different diagnostics complement each other to obtain all this information, and additional analysis with theory and simulation needs to be carried out to identify the cause of the observed time-frequency pattern. However, for detection purposes, a first identification of the modes need to be done with the spectrograms information.

The identification of modes is often complicated by the presence of noise and other artifacts in the spectrograms. The sources of noise can be variate and the object of study for each diagnostic system and experimental device. Sometimes, the noise can have its origin in the diagnostic system itself, external sources (like active diagnostics or heating systems), or it can be an artifact of the signal processing algorithms. In addition, noise can have different patterns: it can be broadband noise, or located ridges in time-frequency, which are indistinguishable to the actual MHD modes. These sources of noise and time-frequency structures need to be acknowledged to detect true mode patterns.

In the later years, a data-driven culture and the use of artificial intelligence have extended all over business and industry. Since the appearance of these disruptive technologies, a research effort has been carried out to apply these innovations to the detection of plasma instabilities. Several works aimed to detect EP driven Alfvén eigenmodes using manually labeled datasets: in COMPASS [9], NSTX [10], DIII-D [11–14]. Particularly, deep learning

segmentation was investigated in TJ-II [15]. Because the spectrograms of plasma diagnostics are images, the application of computer vision algorithms (CV) or deep learning algorithms (DL) is straightforward.

The classic computer vision approach differs from the deep learning approach in several aspects. In a classic CV, the image features are extracted by designing a workflow of algorithms and mathematical models, for example: a composition of wavelet filters can remove grain noise in a photograph. Wavelet transforms are part of the CV algorithms and they are a whole field on its own, and they are extensively used for image compression and manipulation.

These algorithms were developed over years of research, nowadays they require very few computational resources, and they do not require a dataset of images. Their effectiveness relies on assumptions about the image properties, so the mathematical manipulation of the image is deterministic and highly interpretable. For instance, the wavelet strength relies on the acknowledgment of multiscale features in signals and images. However, it is necessary to experiment with different algorithms and their parameters for each image.

In contrast, feature extraction is done automatically in DL models. For instance, using convolutional neural networks (CNNs). In this case, the features are learned using inductive bias, so deep neural networks need to be trained using labeled datasets. Roughly speaking, a CNN can be understood as a concatenation of image filters, in which the parameters are learned using statistics of a given dataset to solve a specific problem. Overall, the fundamental difference between classic CV and DL approaches is the following: in classic CV image features are calculated, and in DL the image features are inferred.

If the amount of data is enough, deep learning can outperform classic CV. However, big image datasets are needed to achieve this advantage, and the performance of DL collapses [16] when the patterns to detect are not present in the training dataset. In addition, computational resources often require multiple GPUs, and the datasets need to be carefully curated before they can be used. For instance, images are down-sampled, centered, and cropped so objects to classify occupy the most image area. Moreover, labeling images is still a highly time-consuming task necessary before DL models can be trained. Therefore, CV and signal processing find their utility when data is scarce or computational resources are constrained, CV is still used in preparing data for deep learning algorithms [17] often enhancing DL performance.

The research on the application of classic CV and wavelet for image processing in Fusion applications is limited. To our knowledge, only previous work [13] from DIII-D uses computer vision algorithms, morphological

filters specifically, to prepare data for using machine learning. For automatic identification of MHD modes: Ridge detection and multi-wavelet convolutional neural networks have been explored in two master theses [18, 19] respectively. This gap in knowledge regarding the use of CV to extract information from plasma spectrograms motivated the research presented in this paper.

This paper is organized as follows. In section 2, the algorithms used in the paper are introduced. The removal of broadband noise and vertical lines from spectrograms is discussed in section 3. Then, we introduce Hough transform to detect straight lines patterns in arbitrary directions in section 4. Following the detection of these objects, sections 5 and 6 are devoted to discussing two methods to remove them in, using 2D-FFT and curvelets respectively. Once, we have explored methods for removing noise, we proceed in section 7 with the segmentation of the spectrogram modes. Finally, section 8 is devoted to the conclusions of the reported work and perspectives beyond the present paper.

2. Spectral algorithms and computer vision

The goal of the presented work is to design a pipeline of algorithms for the segmentation of spectrogram images, identifying the MHD activity in time and frequency separately from noise and other image features. Given an image, the segmentation problem can be defined as the determination of regions of pixels corresponding to different objects. The algorithms used have two differentiated objectives: feature extraction and object detection.

Extracting the features of interest is a previous requisite for the segmentation pipeline to work properly, the steps are: detection of straight lines, removal of straight lines and broadband noise. Once the features are extracted (noise removed), the basic steps for segmentation are ridge detection, automatic thresholding and labelling.

This work uses free and open source software. We have used the PyWavelets implementation [20] for the discrete wavelet transform DWT. The CV algorithms used are available in the Scikit-Image library [21]. Rather than aiming for the tuning of hyperparameters, we compared different algorithm performances with the default parameters, looking for the ones that best adapt to our data features. In addition, this work uses CurveLab implementation, copyrighted by the authors [22], and it is available for academic use. The Python library Curvelops allows Curvelab integration with the rest of the Python workflow.

First, the spectrograms of diagnostic signals are calculated using the discrete version of the short-time Fourier transform (STFFT) given by Scipy implementation. The length of the FFT windows is 2048 samples, the spectral amplitude is given in dB scale. The window function used is the Tukey window. The colormap used is “turbo”, a rainbow colormap similar to “jet”, which was proposed by Google AI research, enhancing value dissimilarities and perceptual uniformity. The rest of parameters are the default library parameters. The images are then resized to 1024 by 1024 pixels before applying the

pipeline.

The discrete wavelet transform is used to remove broadband noise and vertical lines from the spectrograms (section 3): discrete wavelets can be seen as pyramids of multiscale and multidirection filters that decompose and image in filtered sub-images, they are extensively used in image processing to remove noise and extract features. By using discrete wavelet transform (DWT), each image can be decomposed in 4 sub-images: an approximation image, vertical details, horizontal details, and diagonal details. The approximation images are used iteratively to continue the decomposition in the next level as shown in Fig.1. An example of spectrogram decomposition is shown in Fig.2. The approximation image is equivalent to applying a low-pass filter to the columns and a low-pass filter to the rows. That is why the approximation is noted as LL in many sources and it is the notation that we follow in the present paper. Similarly, the vertical details image is equivalent to applying a low-pass filter in the rows and a high-pass filter in the columns (hence the LH notation). The horizontal details image (HL) and diagonal details image (HH) complement the decomposition. In this work, we use the Haar wavelet.

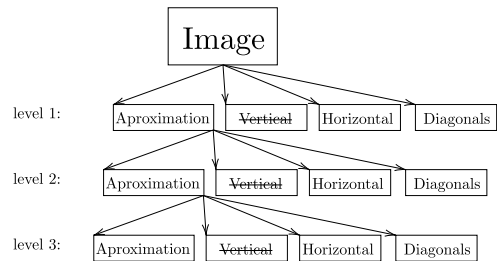


Figure 1. Schematic representation of the wavelet cascade of filters at different levels. Each level includes an approximation image together with vertical, horizontal and diagonal details

The utility of DWT is raised from the fact that the MHD instabilities that can be observed in spectrograms have low spatial frequencies, in other words: low repetition rates across the spectrogram image. While signal noise has high spatial frequencies.

In this paper, we used the Hough transform [23, 24] to detect straight lines $y = mx + b$ in images (section 4). Without entering in all the details: for each pixel point, multiple straight lines represented by $x \cos(\theta) + y \sin(\theta) = \rho$ are considered. Each one is situated at a distance ρ from the origin and the perpendicular to each candidate line forms a θ angle with x-axis. The image is then transformed into a 2D space (Hough space) in which all straight lines are transformed into sine curves. The accumulation of sinusoids in a point of Hough space indicates the presence of a straight line characterized by ρ and θ (Fig.5). It is important to mention that some edge detection (or ridge detection) is needed before running the Hough transform. Otherwise, accumulation points are not clear and the straight line detection might not be efficient enough. For this reason, the Canny edge detector [25] has been used in this case.

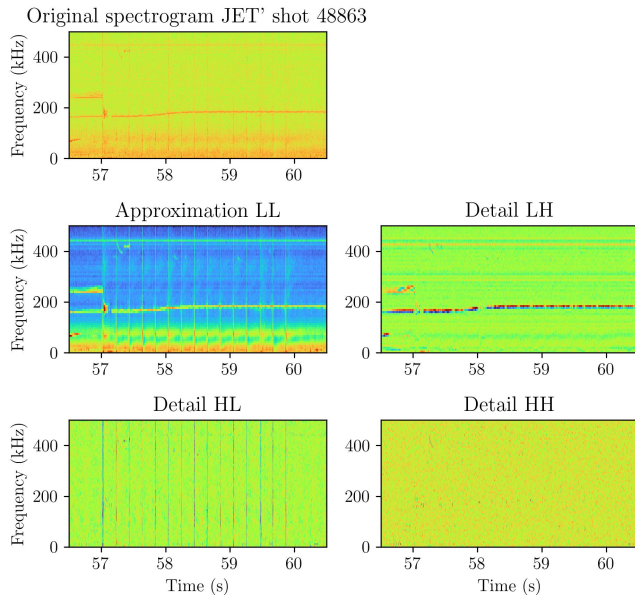


Figure 2. Example of a JET' spectrogram (top) and its third level wavelet decomposition (bottom) composed of the approximation and the horizontal, vertical and diagonal details.

The frequency content of an image can be also studied by extending the definition of the discrete Fourier transform to two dimensions. Many periodic patterns can be detected in the frequency space. For instance, 2D-FFT is used to study crystal structures by X-ray diffraction. The main application of the two-dimensional Fourier transform in computer vision is the manipulation of the image in the frequency space using masks. In this paper, 2D-FFT is employed for filtering spectral components in a desired direction (section 5). The implementation of the 2D Fourier transform can be found in Python's Numpy library.

The discrete wavelet decomposition of images is a powerful tool for denoising and extracting features [26–31]. However, the number of directions might be too coarse in some scenarios. For instance, a vertical and horizontal multiscale pattern could not be enough to describe curved ridges filling the image space. Likewise can happen with MHD activity on spectrograms. The lack of directionality of DWT motivated the development of the curvelet transform [22, 32], which are employed in the present work to extend the results with DWT (section 3) to many directions (section 6)

The fast Curvelet transform [22] is based on partitioning the Fourier space: A tessellation of windows (wedges) applied to the Fourier space creates a multi-scale, multi-directional filter bank. The fast Curvelet transform of an image $f(x_1, x_2)$ can be defined as

$$\begin{aligned} & \text{Curvelet transform}\{f(x_1, x_2)\} \\ &= \sum_{\text{scales}} \sum_{\text{angles}} \langle f, \phi_{\text{scale, angle}} \rangle \phi_{\text{scale, angle}}, \end{aligned} \quad (1)$$

where $\langle f, \phi_{\text{scale, angle}} \rangle$ is the weight corresponding to the wedge $\phi_{\text{scale, angle}}$ in Fourier space [22].

Finally, the algorithms used to perform the segmentation (section 7) are: the ridge Sato's filter [33] with scales $\sigma_{\text{scales}} = [1, 2]$ to detect mode ridges in the spectrograms; the Yen's automatic thresholding algorithm [34] which is used to separate signal from noise and binarize the spectrogram images. Finally, a pixel connectivity filter [35, 36] is used to label separated elements in the binary images. The algorithm parameters are the Scikit-Image library default ones [21].

3. Broadband noise removal using discrete wavelet transforms

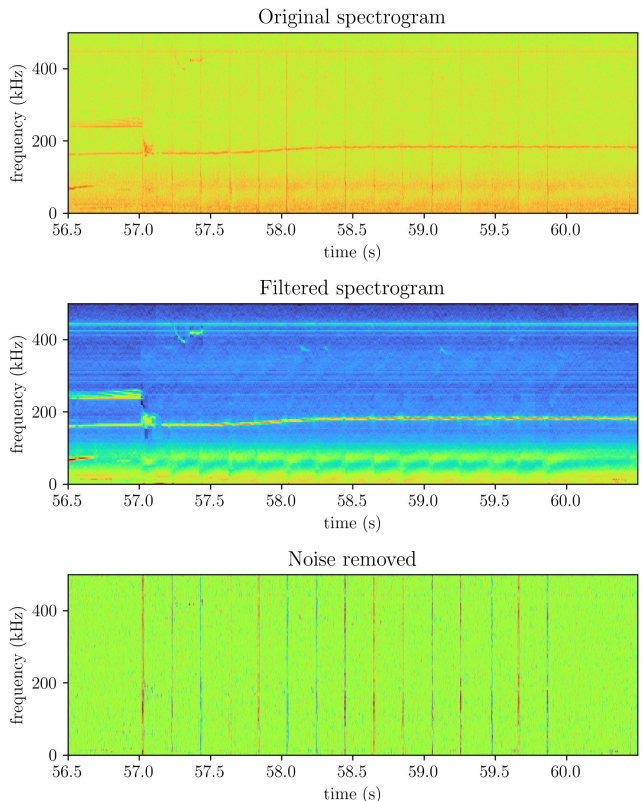


Figure 3. Example of broadband spectral noise removal on JET's shot 48863. Clips caused by pellets injections are removed from the spectrogram, leaving only MHD activity in the image. TAEs and EAEs are then easily observed.

In JET shot in Fig.3 we can see various toroidal Alfvén eigenmodes (TAE) over 200 kHz at the between 0 and 0.5 s approximately. Then 15 periodic pellet injections fuel the plasma (they can be distinguished by the vertical lines in the spectrogram). The pellet injections fundamentally increase plasma density and reduce its temperature. It can be seen in the first pellet injection just after 0.5 (s), how they affect the TAE modes. As the density increases abruptly, the TAE frequency $f_{\text{TAE}} \propto 1/\sqrt{n}$ decreases, and then the TAE disappears soon afterward. A similar effect can be observed on an elliptical Alfvén eigenmode (EAE) at ≈ 420 kHz and ≈ 0.9 s. More deeply, the effect of pellet injection is a modification of the Alfvén continuum

spectrum, which is studied in [37] with shots similar to the one showed in Fig.3.

The time series signals from JET magnetic diagnostics have abundant spikes and discontinuities. It is well known that the Fourier transform has difficulties in representing non-differentiable or non-stationary time series, producing Gibbs artifacts in the signal's reconstruction and spectral leakage in the frequency space. The classic example is the Fourier transform of a square signal in which ripples are present at the edges of the square reconstruction, the decomposition of sines and cosines used by FFT struggles to recreate this type of signal. A dramatic example is the Fourier transform of a unit impulse (dirac's delta $\delta(\tau = 0)$), which requires infinite frequencies to reconstruct the pulsed signal. Because these patterns are present in diagnostics signals, JET's time-frequency spectrograms have abundant broadband noise.

The character of spectrograms noise is highly anisotropic, due to the spectral leakage of the STFFT on each time window. This broadband noise is located mostly in the vertical details sub-image. Therefore removing the vertical details of the image allows us to clean the spectrograms. When vertical details pixels (all levels of vertical sub-images, as indicated in Fig.1) are set to zero and the inverse DWT is applied, broadband spectral noise is significantly reduced. An example is shown in Fig.3 (including pellet injection events of this particular example). The steps are summarized in the algorithm (1).

Approximation and horizontal details subimages are left unchanged. In addition, some high-frequency noise is present in the diagonal subimages, so they have a soft thresholding (all pixel values in diagonal subimages are multiplied by $\alpha_D = 0.5$).

Algorithm 1: Remove broadband noise, clics and pops from spectrogram

Input: Time series \mathbf{s}

Parameters: Levels deep: $N=8$

Vertical threshold: $\alpha_V = 0$,

diagonal threshold: $\alpha_D = 0.5$

Output: Reassigned spectrogram $S_{xx(mod)}$

Steps:

- 1 Obtain spectrogram matrix S_{xx} using STFFT(\mathbf{s}).
 - 2 Workout DWT tree.
 - 3 Set $\alpha_V = 0$ in all vertical details images in levels 1:N (hard thresholding).
 - 4 Set $\alpha_D = 0.5$ in all diagonal details images in level 1:N (soft thresholding).
 - 5 Use inverse DWT to generate a filtered spectrogram.
-

It is worth mentioning that keeping one of the first approximation sub-images can also result in a spectrogram with an improved signal-to-noise ratio, though omitting details sub-images could produce modes with coarser details.

The maximum number of levels that can be calculated

depends on the number of pixels in the image, the more pixels, the more levels can be calculated. Given an optimal time-frequency uncertainty, determined by the window size in the STFFT. One way of increasing the number of pixels in the spectrogram is allowing more overlapping of time windows. The maximum number of levels can be determined by the appearance of border effects, and we calculate all levels possible.

4. Straight line pattern detection

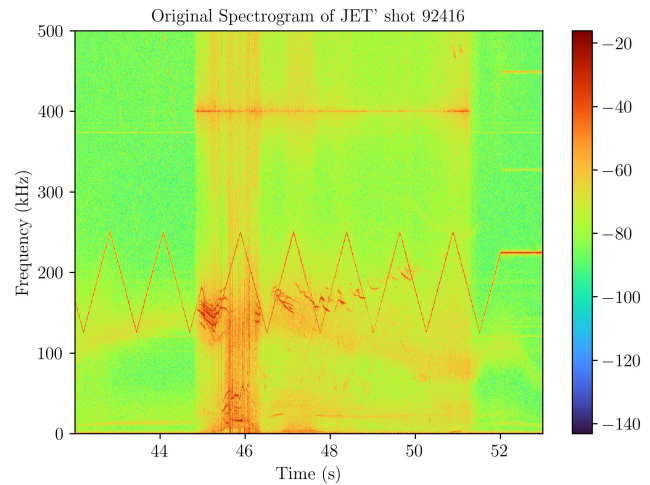


Figure 4. Spectrogram of JET shot 92416.

Some signals observed in spectrograms are straight lines with certain orientations. In many cases, these signals are not caused by plasma instabilities. For instance, the TAE antenna creates the frequency sweeping pattern that can be observed in Fig.4. The shot 92416 is an afterglow experiment studied in detail [38]. To remove the straight line patterns shown in this shot, we need to generalize the result obtained with the pellet signals to other directions different than the vertical.

It is to be expected that the pellet's injections time or requested TAE antenna frequencies are available in the shot database. However, side lobes (harmonics) of the TAE antenna signal can appear.

Before applying the Hough transform, it is necessary to enhance the edges in the spectrogram image. The Canny edge detector is used for this purpose. Then, the Hough transform expresses the image in its own space. The accumulation of overlapping sinusoids over a point creates bright regions in Fig.5, providing evidence of a straight line. Note how some curves converge to points at ± 90 degrees (horizontal lines in images), and around ± 10 degrees (antenna sweep).

The result of the straight-line detection is shown in Fig.6. The angles detected are centered around 0.39 ± 1.63 , 77.59 ± 2.63 , 83.1 ± 1.63 , 95.97 ± 2.01 , 103.32 ± 2.61 , and 179.61 ± 1.65 (in degrees). In addition, it is worth mentioning that probabilistic Hough transform [24] can be used to add priors like line length, angular orientation, or

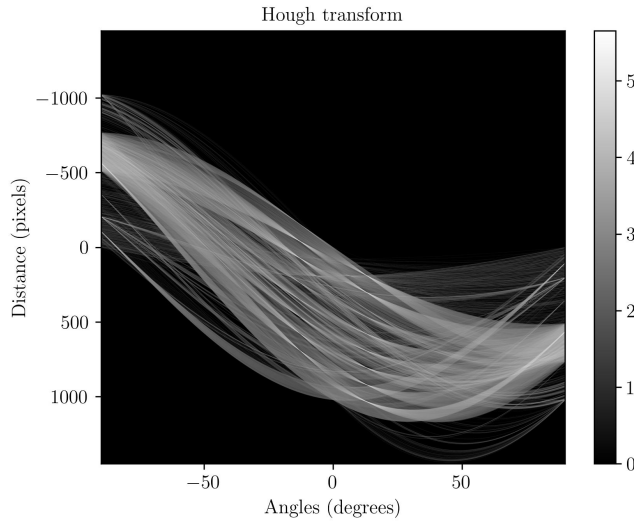


Figure 5. Result of Hough transform. The accumulation of sinusoids passing through a point indicates the presence of a straight line in the image space.

separation between lines. The result is shown in Fig.7. This extends further applications of the Hough transform.

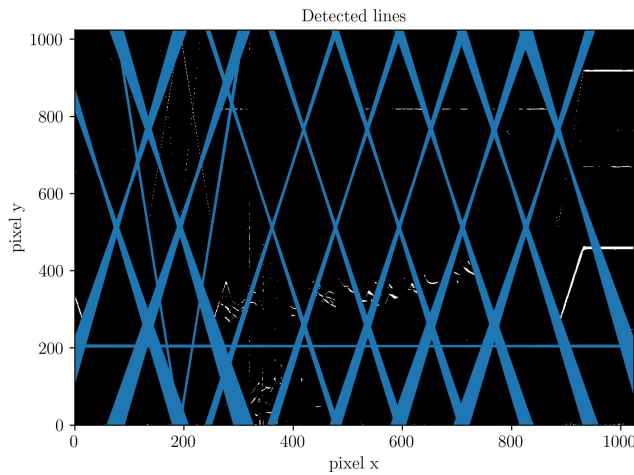


Figure 6. Result of Hough transform analysis showing the straight lines detected.

5. Removal of oriented patterns using 2D FFT

To proceed with the removal of oriented patterns, we start with the straight lines detected using Hough transform (corresponding to the TAE antenna sweep). Our first approach would be to transform the spectrogram's image $f(x_1, x_2)$ to the Fourier space $F(k_1, k_2)$. The steps are summarized in the algorithm (2).

The Fourier space contains the image information expressed as spatial frequencies along the two image directions. Then a mask over the magnitude spectrum can be designed to remove all frequencies along the

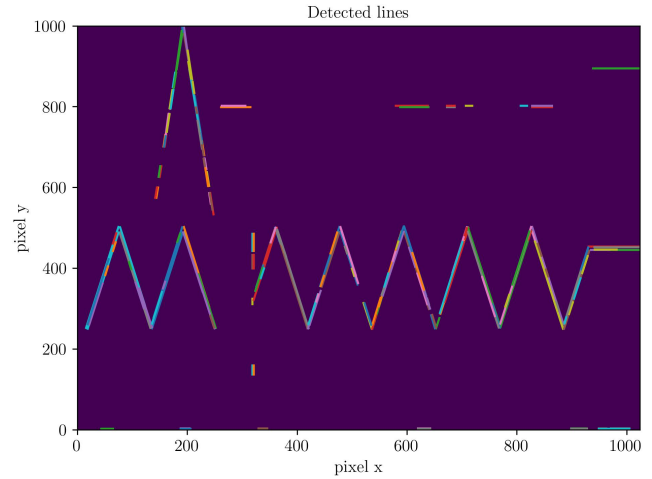


Figure 7. Result of probabilistic Hough transform. Prior length is 12 pixels.

desired directions. Note that the FFT2D rotates the straight line angles $\pi/2$ or 90° detected with the Hough transform, for instance lines detected at 77.59° generate features at $77.59^\circ - 90^\circ = 12.4^\circ$ in the Fourier space. The supplementary angles of $\pm 12^\circ$ are $12.4^\circ + 180^\circ = 192.4^\circ$ and $-12^\circ + 180^\circ = 167.6^\circ$.

Therefore, the mask angles used in this example are $\theta = [\theta_1, \theta_2, \theta_3, \theta_4] = [12.4^\circ, -12.4^\circ, 192.4^\circ, 167.6^\circ]$. Then, the angular mask widths are set to $\Delta\theta = [\Delta\theta_1, \Delta\theta_2, \Delta\theta_3, \Delta\theta_4] = [8^\circ, 8^\circ, 8^\circ, 8^\circ]$. In addition, the radial mask is set so it reaches the end of the Fourier 2D space, so the mask cut-off is $\delta = [\delta_1, \delta_2, \delta_3, \delta_4] = [1024, 1024, 1024, 1024]$.

The inverse Fourier transform applied to the masked spectra generates an image free from features along these angles. The result of the inverse 2D FFT is given in a complex number matrix, so the real part (or the absolute value) of this matrix needs to be taken in order to plot the spectrogram. Taking the real part preserves the original dynamic range of the spectrogram (colors) removing the TAE antenna signal as shown in in Fig.8. It is to be noted that the amplitude values are modified (observe the colorbars scale in Fig.8). Taking the absolute value gives a similar result, but it might return a negative image, therefore changing the color range of Fig.8).

To summarize, Fig.8 shows the original spectra, the 2D FFT magnitude spectrum while a filter mask, the resulting spectrogram, and the features removed from the images: the TAE antenna signal is successfully removed from the spectrogram. It is to be noted that removing these directions keeps most information of the original signal (sawteeth or MHD activity can not be observed in the removed features). However, modes aligned with these directions can be attenuated or disappear.

If algorithms (1) and (2) are combined, the resulting image offers an improved contrast highlighting MHD features of the signal. In Fig.9 most of broadband noise and the complete TAE antenna signal are removed. However, this approach is not without limitations. If the MHD

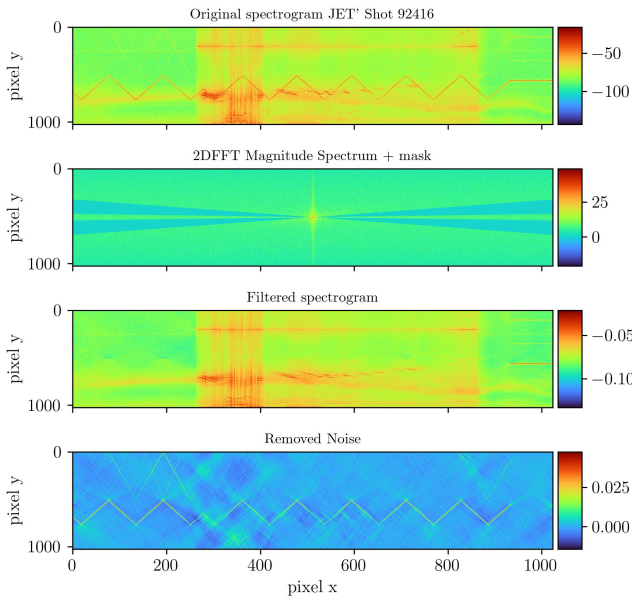


Figure 8. Use of 2D FFT to remove TAE antenna sweeps: Original image, Mask over 2D FFT, Filtered image, and noise removed.

Algorithm 2: Remove straight line patter using 2D FFT high pass directional filters

Input: Time series \mathbf{s}

Parameters:

Mask angles: $\boldsymbol{\theta} = [\theta_1, \dots, \theta_N]$.

Angle width: $\Delta\boldsymbol{\theta} = [\Delta\theta_1, \dots, \Delta\theta_N]$.

Mask cut-off: $\boldsymbol{\delta} = [\delta_1, \dots, \delta_N]$

Output: Reassigned spectrogram $S_{xx(mod)}$

Steps:

- 1 Obtain spectrogram matrix S_{xx} using STFFT(\mathbf{s}).
 - 2 Resize image S_{xx} to have squared size: 1024×1024 .
 - 3 Transform resized image to frequency space.
 - 4 Apply Mask to frequency space (truncated circle sectors centered at θ_i , width $\Delta\theta_i$, and maximum radius δ_i).
 - 5 Inverse transform the masked image to obtain the filtered image $S_{xx(mod)}$.
 - 6 Return $\text{Re}\{S_{xx(mod)}\}$
-

activity aligns with the TAE antenna sweeps, we might lose these modes. For instance, two elliptic alfvén eigenmodes (EAE)s disappear, these small modes are situated at 51s and 475 kHz approximately (decreasing in frequency). Moreover, sawteeth signals are still crossing the MHD modes.

The design of the mask might need some trial and error in selecting the parameters. In the 2D FFT low frequencies are situated in the center. In order to not cover this region, the mask is a composition of radial circle sectors

centered at angles $\boldsymbol{\theta}$ with respective apertures $\Delta\boldsymbol{\theta}$. The mask starts at a radial cut-off $\boldsymbol{\delta}$ distance from the origin, so low spatial-frequencies are not filtered. In addition, it is been found useful to resize the spectrogram to a square image in advance. This helps to design a symmetric mask (the radial mask apertures $\Delta\boldsymbol{\theta}$ are centered around the given angles $\boldsymbol{\theta}$).

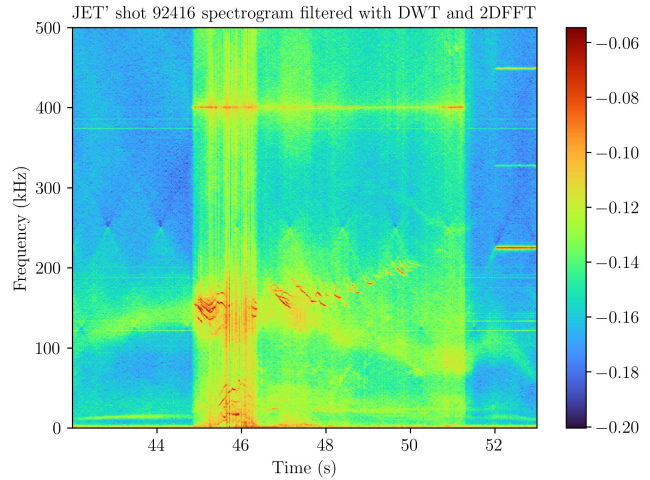


Figure 9. Result of combining Algorithm 1 and 2. On the left the original spectrogram is shown, in the right picture the result of using both algorithms.

The manipulation of Fourier space is a key concept to understanding curvelet transform as well. Given the success of using discrete wavelets in the algorithm (1) we worked on generalizing this approach by using curvelets.

6. Multiscale-multidirection pattern removal using curvelets

The curvelet transform [22] is a multidirectional generalization of the DWT, better suited when images have curvy edges and multiple directional features, like the MHD modes in our spectrograms. For removing noise and undesired components in a selected angular direction, corresponding subimages are set 0 and then the inverse curvelet transform is applied.

In Fig.10, a polar representation of the 2D Fourier space is shown. The 2D Fourier space is divided in a tessellation of “wedges” [22]. Each wedge has a corresponding subimage with certain scale and directional properties. The wedges closer to the center are subimages with large scale (low-frequency) features. The colored wedges are the ones selected to be removed before the inverse Curvelet transform is applied. These directions are vertical, horizontal, and the corresponding directions of the antenna sweeping. The scales to be removed in these directions are everyone but the corresponding to the two larger scales (lower frequencies represented in the center wedge, and the first concentric wedges).

The result of using the algorithm (3) steps 1-3 can be seen in Fig.11, the noise removed is plotted on Fig.12. Curvelets are able to remove anisotropic noise and improve

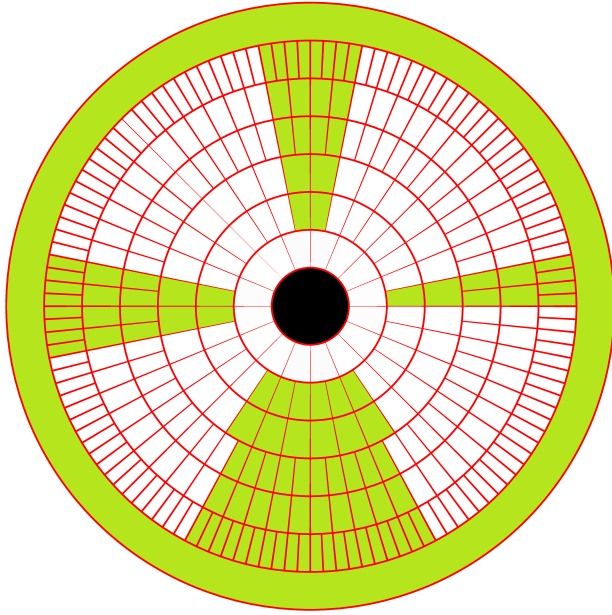


Figure 10. Cartoon of curvelet's wedges in polar coordinates. Colored wedges are set to zero before doing the inverse Curvelet transform

spectrogram contrast. Moreover, the TAE antenna signal and the ICRH subharmonics are successfully removed from the spectrogram, sawteeth are eliminated as well. The wedge tessellation is configured by selecting the number of scales and wedges corresponding to the angles detected with the Hough transform. The interested reader can find more details about the curvelet transform in Ma's review paper [32].

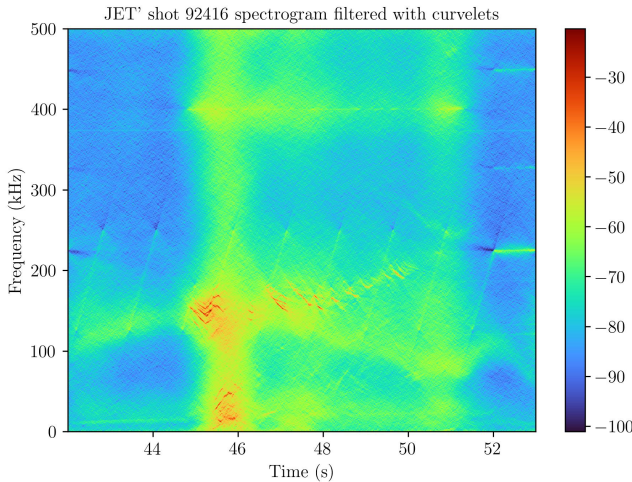


Figure 11. Result of applying curvelet transform algorithm to remove TAE antenna: Algorithm (3), steps: 1-3.

It is worth mentioning that although the all examples in this paper are originating from magnetic sensor signals, these noise removal algorithms could be useful with

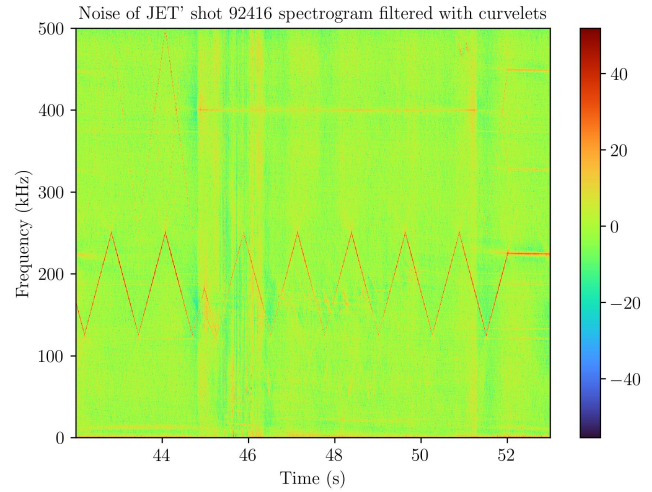


Figure 12. Noise extracted using curvelets

interferometers or LIDAR diagnostic signals as well, which particularly can suffer from straight lines artifacts caused by phase jumps.

7. Automatic identification of MHD modes

Algorithm 3: Complete pipeline for automatic labeling of MHD activity

Input: Time series \mathbf{s}

Parameters: $\sigma = 1$, $\sigma_{\text{scales}} = [1, 2]$,
 $\boldsymbol{\theta} = [\theta_1, \dots, \theta_N]$, $\zeta=9$ (optional)

Output: Reassigned spectrogram $S_{xx(mod)}$

Steps:

- 1 Calculate the spectrogram STFFT(\mathbf{s});
 - 2 Detect straight line patterns or specify angles manually.
 - 3 Apply curvelet transform (or use Algorithm 2 and skip steps 4 and 5).
 - 4 Set to 0 (hard thresholding) wedges corresponding to directions $\boldsymbol{\theta}$
 - 5 Apply inverse curvelet transform, take the absolute value and invert the image.
 - 6 Apply Sato's ridge operator with $\sigma_{\text{scales}} = [1, 2]$. (Or Meijering's)
 - 7 Smoothing: Gaussian($\sigma=1$).
 - 8 Yen's automatic thresholding (binarize the image).
 - 9 Mark up pixel-connected areas (for labelling MHD activity), using a full-connectivity filter
 - 10 Removed noisy labels: modes with less than $\zeta=9$ pixels. (Optional)
-

After improving contrast and having removed other undesired signal components, classic CV algorithms can

perform optimally labeling the MHD activity, using all the steps indicated in the algorithm (3).

Given the result of Fig.11: Sato's ridge operator can be applied to detect the mode pixels. It is worth mentioning that the Meijering's ridge filter [39] can perform as well or better than Sato's. Afterwards, a Gaussian smoothing of 1 pixel width is applied to remove some background smearing texture left by the Ridge operator. Finally, Yen's automatic thresholding is used to binarize the image: the pixel values are 0 or 1.

Then, it is easy to detect connected areas by using a connectivity filter. When two pixels are next to each other and have the same value, they are linked. In a 2-connectivity filter (full), diagonal linking is allowed, whereas in a 1-connectivity filter, only vertical and horizontal-vertical linking is permitted. To give some examples, in a 3×3 image, among all combinations, 5 connected pixels variation on a binarized image can be

$$\begin{bmatrix} 1 & 0 & 0 \\ 1 & 0 & 0 \\ 1 & 1 & 1 \end{bmatrix}, \begin{bmatrix} 0 & 1 & 0 \\ 1 & 1 & 1 \\ 0 & 1 & 0 \end{bmatrix}, \begin{bmatrix} 1 & 0 & 1 \\ 0 & 1 & 0 \\ 1 & 0 & 1 \end{bmatrix}.$$

Next step is optional (remove noisy labels). We can considered noisy modes: those with less than 9 pixels connected. In other words, a labelled mode is noisy if a mode is a pixel not fully linked with surroundings. This criteria can vary depending on the number of pixels in the spectrogram and the size of the modes.

Algorithm (3) result in Fig.13. We conclude that individual modes are successfully labeled with minor errors like a few modes missed and only three false positives out of 45 regions of pixels detected. In addition, some modes of very low signal-to-noise ratio and mostly aligned with the removed directions are missed.

It is to be noted that an application with a graphical user interface could be used to discard these minor labeling errors. For instance, a tool called *Wavystar* with a GUI has been implemented, available under request in JET. This application implements algorithms discussed in this work, and other analysis capabilities of transitory signals not treated in this paper.

We conclude by mentioning that the computational resources needed to run these algorithms are very low. A common laptop (11th Gen Intel(R) Core(TM) i7-1185G7, 3.00GHz) can run these algorithms in a few seconds without special memory requirements (16-32 GB RAM). Also, the presented algorithms have few hyper-parameters. These facts make them suitable for mining big databases.

8. Conclusion and future work

The main innovation introduced in this work is the use of wavelets and curvelets along with simple CV algorithms to filter (reassign) the spectrograms of magnetic sensors. The complete pipeline successfully removes noise and undesired patterns in a fully interpretable way, in other words the addition of removed noise and filtered spectrogram returns the original signal.

The main concepts that allowed these results are two:

(1) noise present in spectrograms is highly anisotropic,

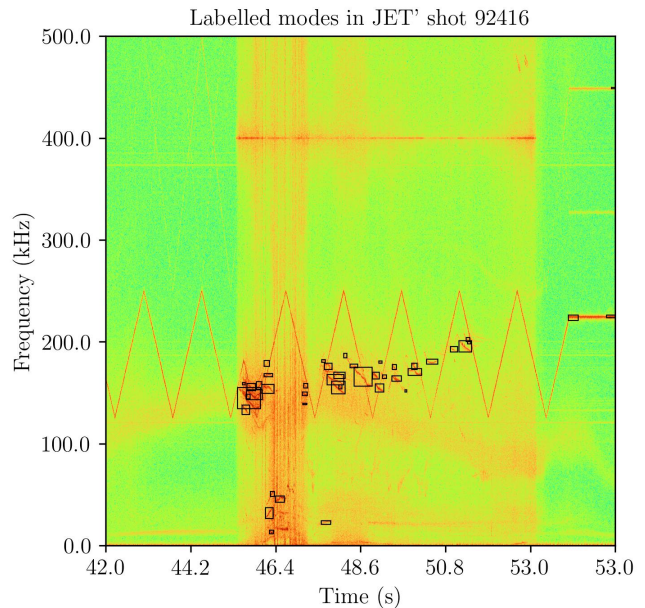


Figure 13. Result of automatic labelling over original spectrogram. In total, 43 modes are segmented correctly. After 53 s, part of the TAE antenna signal produces 3 false positives.

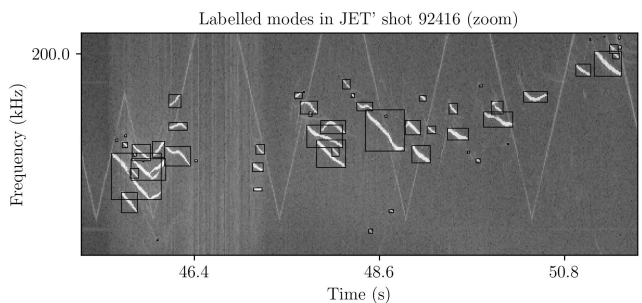


Figure 14. Detail of the result of automatic labeling

and (2) the plasma phenomena observed in spectrograms are multi-scale. Therefore, removing features in a certain scale and direction maintains a high fraction of the original information containing the MHD modes.

Nowadays, the state of the art in computer vision algorithms is the use of deep CNNs and other neural network architectures. However, they require huge amounts of curated data. The application of classic computer vision algorithms has not been extensively researched in Fusion applications, which constitutes a gap of knowledge that this work aims to fill. The application of these classic algorithms is a necessary step for creating curated datasets, improving the performance of future deep learning algorithms.

Data contained in spectrograms, like frequencies, duration, and amplitudes of the MHD modes, can be extracted, stored and further studied. A straightforward application of the algorithms introduced in this paper is the creation and curation of a database of modes. Finally, the database obtained can be used to train DL networks for real-time mode prediction.

Acknowledgments

All **CurveLab** commercial rights are reserved to [22] authors, though it is freely available for academic use. The algorithms presented here only call CurveLab functions through the open-sourced Python library **curvelops**.

This work has been carried out within the framework of the EUROfusion Consortium, funded by the European Union via the Euratom Research and Training Programme (Grant Agreement No 101052200-EUROfusion). Views and opinions expressed are however those of the author(s) only and do not necessarily reflect those of the European Union or the European Commission. Neither the European Union nor the European Commission can be held responsible for them.

This work has received financial support from the AIM4EP project (ANR-21-CE30-0018), funded by the French National Research Agency (ANR) and from the Aix-Marseille University Initiative of Excellence - A*Midex, Investissements d'Avenir programme AMX-19-IET-013.

This work has received funding under the Implementing Agreement No. 2 to the Agreement on Academic and Scientific Cooperation (REF. : AMUDRVCP09052019-1 / 4300002670) between the ITER International Fusion Energy Organization and Aix-Marseille University. The views and opinions expressed herein do not necessarily reflect those of the ITER Organization.

References

1. Heidbrink, W. W. Basic physics of Alfvén instabilities driven by energetic particles in toroidally confined plasmas. en. *Physics of Plasmas* **15**, 055501. ISSN: 1070-664X, 1089-7674. doi:[10.1063/1.2838239](https://doi.org/10.1063/1.2838239) (May 2008).
2. Gorelenkov, N., Pinches, S. & Toi, K. Energetic particle physics in fusion research in preparation for burning plasma experiments. en. *Nuclear Fusion* **54**, 125001. ISSN: 0029-5515, 1741-4326. doi:[10.1088/0029-5515/54/12/125001](https://doi.org/10.1088/0029-5515/54/12/125001) (Dec. 2014).
3. Sharapov, S. *et al.* Energetic particle instabilities in fusion plasmas. en. *Nuclear Fusion* **53**, 104022. ISSN: 0029-5515, 1741-4326. doi:[10.1088/0029-5515/53/10/104022](https://doi.org/10.1088/0029-5515/53/10/104022) (Oct. 2013).
4. Mirnov, S. V. & Semenov, B. THE NATURE OF THE LARGE-SCALE INSTABILITIES IN THE TOKAMAK. en. *Soviet Physics JETP* **33**, 1134 (1974).
5. Van Zeeland, M. A. *et al.* Radial Structure of Alfvén Eigenmodes in the DIII-D Tokamak through Electron-Cyclotron-Emission Measurements. en. *Physical Review Letters* **97**, 135001. ISSN: 0031-9007, 1079-7114. doi:[10.1103/PhysRevLett.97.135001](https://doi.org/10.1103/PhysRevLett.97.135001) (Sept. 2006).
6. Freethy, S. J. *et al.* Measurement of turbulent electron temperature fluctuations on the ASDEX Upgrade tokamak using correlated electron cyclotron emission. en. *Review of Scientific Instruments* **87**, 11E102. ISSN: 0034-6748, 1089-7623. doi:[10.1063/1.4958908](https://doi.org/10.1063/1.4958908) (Nov. 2016).
7. Nazikian, R. *et al.* Alpha-Particle-Driven Toroidal Alfvén Eigenmodes in the Tokamak Fusion Test Reactor. en. *Physical Review Letters* **78**, 2976–2979. ISSN: 0031-9007, 1079-7114. doi:[10.1103/PhysRevLett.78.2976](https://doi.org/10.1103/PhysRevLett.78.2976) (Apr. 1997).
8. Sharapov, S. *et al.* Alfvén cascades in JET discharges with NBI-heating. en. *Nuclear Fusion* **46**, S868–S879. ISSN: 0029-5515, 1741-4326. doi:[10.1088/0029-5515/46/10/S02](https://doi.org/10.1088/0029-5515/46/10/S02) (Oct. 2006).
9. Škvára, V. *et al.* Detection of Alfvén Eigenmodes on COMPASS with Generative Neural Networks. *Fusion Science and Technology* **76**. Publisher: Taylor & Francis eprint: <https://doi.org/10.1080/15361055.2020.1820805>, 962–971. ISSN: 1536-1055. doi:[10.1080/15361055.2020.1820805](https://doi.org/10.1080/15361055.2020.1820805) (Nov. 2020).
10. Woods, B. J. Q. *et al.* Machine Learning Characterization of Alfvénic and Sub-Alfvénic Chirping and Correlation With Fast-Ion Loss at NSTX. *IEEE Transactions on Plasma Science* **48**. Conference Name: IEEE Transactions on Plasma Science, 71–81. ISSN: 1939-9375. doi:[10.1109/TPS.2019.2960206](https://doi.org/10.1109/TPS.2019.2960206) (Jan. 2020).
11. Jalalvand, A. *et al.* Alfvén eigenmode classification based on ECE diagnostics at DIII-D using deep recurrent neural networks. en. *Nuclear Fusion* **62**. Publisher: IOP Publishing, 026007. ISSN: 0029-5515. doi:[10.1088/1741-4326/ac3be7](https://doi.org/10.1088/1741-4326/ac3be7) (Dec. 2021).
12. Jalalvand, A. *et al.* Alfvén eigenmode classification based on ECE diagnostics at DIII-D using deep recurrent neural networks. *Nuclear Fusion* **62**, 026007. ISSN: 0029-5515, 1741-4326. doi:[10.1088/1741-4326/ac3be7](https://doi.org/10.1088/1741-4326/ac3be7) (Feb. 2022).
13. Kaptanoglu, A. A. *et al.* Exploring data-driven models for spatiotemporally local classification of Alfvén eigenmodes. *Nuclear Fusion* **62**, 106014. ISSN: 0029-5515, 1741-4326. doi:[10.1088/1741-4326/ac8a03](https://doi.org/10.1088/1741-4326/ac8a03) (Oct. 2022).
14. Garcia, A. V. *et al.* Alfvén eigenmode detection using Long-Short Term Memory Networks and CO_2 Interferometer data on the DIII-D National Fusion Facility in 2023 International Joint Conference on Neural Networks (IJCNN) (IEEE, Gold Coast, Australia, June 2023), 1–8. ISBN: 978-1-66548-867-9. doi:[10.1109/IJCNN54540.2023.10191760](https://doi.org/10.1109/IJCNN54540.2023.10191760).

15. Bustos, A., Ascasíbar, E., Cappa, A. & Mayo-García, R. Automatic identification of MHD modes in magnetic fluctuation spectrograms using deep learning techniques. en. *Plasma Physics and Controlled Fusion* **63**. Publisher: IOP Publishing, 095001. ISSN: 0741-3335. doi:[10.1088/1361-6587/ac08f7](https://doi.org/10.1088/1361-6587/ac08f7) (July 2021).
16. Ofir, N. & Nebel, J.-C. *Classic versus deep learning approaches to address computer vision challenges*. arXiv:2101.09744 [cs]. Oct. 2021.
17. O'Mahony, N. *et al.* en. in *Advances in Computer Vision* (eds Arai, K. & Kapoor, S.) Series Title: Advances in Intelligent Systems and Computing, 128–144 (Springer International Publishing, Cham, 2020). ISBN: 978-3-030-17794-2 978-3-030-17795-9. doi:[10.1007/978-3-030-17795-9_10](https://doi.org/10.1007/978-3-030-17795-9_10).
18. Colvin, J. L. Automated tracing of divergent ridges in tokamak magnetic spectra. en. *Master thesis* (2023).
19. Oroumchian, N. ECEI Spectrogram Denoising and Feature Extraction using a Multi-Wavelet Convolutional Neural Network Model. en. *Master thesis*. doi:[MerrittID : ark : /13030 / m5h52mx2](https://doi.org/MerrittID:ark:/13030/m5h52mx2) (2023).
20. Lee, G., Gommers, R., Waselewski, F., Wohlfahrt, K. & O'Leary, A. PyWavelets: A Python package for wavelet analysis. *Journal of Open Source Software* **4**, 1237. ISSN: 2475-9066. doi:[10.21105/joss.01237](https://doi.org/10.21105/joss.01237) (Apr. 2019).
21. Van Der Walt, S. *et al.* scikit-image: image processing in Python. en. *PeerJ* **2**, e453. ISSN: 2167-8359. doi:[10.7717/peerj.453](https://doi.org/10.7717/peerj.453) (June 2014).
22. Candès, E., Demanet, L., Donoho, D. & Ying, L. Fast Discrete Curvelet Transforms. en. *Multiscale Modeling & Simulation* **5**, 861–899. ISSN: 1540-3459, 1540-3467. doi:[10.1137/05064182X](https://doi.org/10.1137/05064182X) (Jan. 2006).
23. Duda, R. O. & Hart, P. E. Use of the Hough transformation to detect lines and curves in pictures. en. *Communications of the ACM* **15**, 11–15. ISSN: 0001-0782, 1557-7317. doi:[10.1145/361237.361242](https://doi.org/10.1145/361237.361242) (Jan. 1972).
24. Galamhos, C., Matas, J. & Kittler, J. *Progressive probabilistic Hough transform for line detection in Proceedings. 1999 IEEE Computer Society Conference on Computer Vision and Pattern Recognition (Cat. No PR00149)* (IEEE Comput. Soc, Fort Collins, CO, USA, 1999), 554–560. ISBN: 978-0-7695-0149-9. doi:[10.1109/CVPR.1999.786993](https://doi.org/10.1109/CVPR.1999.786993).
25. Canny, J. A Computational Approach to Edge Detection. *IEEE Transactions on Pattern Analysis and Machine Intelligence* **PAMI-8**, 679–698. ISSN: 0162-8828. doi:[10.1109/TPAMI.1986.4767851](https://doi.org/10.1109/TPAMI.1986.4767851) (Nov. 1986).
26. Oroumchian, N. ECEI Spectrogram Denoising and Feature Extraction using a Multi-Wavelet Convolutional Neural Network Model. en.
27. Gyaourova, A., Kamath, C. & Fodor, I. K. *Undecimated Wavelet Transforms for Image De-noising*. en. Tech. rep. UCRL-ID-150931, 15002085 (Nov. 2002), UCRL-ID-150931, 15002085. doi:[10.2172/15002085](https://doi.org/10.2172/15002085).
28. Sankur, B. Survey over image thresholding techniques and quantitative performance evaluation. en. *Journal of Electronic Imaging* **13**, 146. ISSN: 1017-9909. doi:[10.1117/1.1631315](https://doi.org/10.1117/1.1631315) (Jan. 2004).
29. Bnou, K., Raghay, S. & Hakim, A. A wavelet denoising approach based on unsupervised learning model. en. *EURASIP Journal on Advances in Signal Processing* **2020**, 36. ISSN: 1687-6180. doi:[10.1186/s13634-020-00693-4](https://doi.org/10.1186/s13634-020-00693-4) (Dec. 2020).
30. Kimlyk, M. & Umnyashkin, S. *Image denoising using discrete wavelet transform and edge information in 2018 IEEE Conference of Russian Young Researchers in Electrical and Electronic Engineering (EIConRus)* (IEEE, Moscow, Jan. 2018), 1823–1825. ISBN: 978-1-5386-4339-6 978-1-5386-4340-2. doi:[10.1109/EIConRus.2018.8317461](https://doi.org/10.1109/EIConRus.2018.8317461).
31. Tuba, U. & Zivkovic, D. *Image Denoising by Discrete Wavelet Transform with Edge Preservation in 2021 13th International Conference on Electronics, Computers and Artificial Intelligence (ECAI)* (IEEE, Pitesti, Romania, July 2021), 1–4. ISBN: 978-1-66542-534-6. doi:[10.1109/ECAI52376.2021.9515079](https://doi.org/10.1109/ECAI52376.2021.9515079).
32. Ma, J. & Plonka, G. The Curvelet Transform. *IEEE Signal Processing Magazine* **27**, 118–133. ISSN: 1053-5888. doi:[10.1109/MSP.2009.935453](https://doi.org/10.1109/MSP.2009.935453) (Mar. 2010).
33. Sato, Y. *et al.* Three-dimensional multi-scale line filter for segmentation and visualization of curvilinear structures in medical images. en. *Medical Image Analysis* **2**, 143–168. ISSN: 13618415. doi:[10.1016/S1361-8415\(98\)80009-1](https://doi.org/10.1016/S1361-8415(98)80009-1) (June 1998).
34. Yen, J.-C., Chang, F.-J. & Chang, S. A new criterion for automatic multilevel thresholding. *IEEE Transactions on Image Processing* **4**. Conference Name: IEEE Transactions on Image Processing, 370–378. ISSN: 1941-0042. doi:[10.1109/83.366472](https://doi.org/10.1109/83.366472) (Mar. 1995).

35. Wu, K., Otoo, E. & Shoshani, A. *Optimizing connected component labeling algorithms in Medical Imaging 2005: Image Processing* **5747** (SPIE, Apr. 2005), 1965–1976. doi:[10.1117/12.596105](https://doi.org/10.1117/12.596105).
36. Fiorio, C. & Gustedt, J. Two linear time Union-Find strategies for image processing. en. *Theoretical Computer Science* **154**, 165–181. ISSN: 03043975. doi:[10.1016/0304-3975\(94\)00262-2](https://doi.org/10.1016/0304-3975(94)00262-2) (Feb. 1996).
37. Oliver, H. *et al.* Modification of the Alfvén wave spectrum by pellet injection. en. *Nuclear Fusion* **59**, 106031. ISSN: 0029-5515, 1741-4326. doi:[10.1088/1741-4326/ab382b](https://doi.org/10.1088/1741-4326/ab382b) (Oct. 2019).
38. Fitzgerald, M. *et al.* Toroidal Alfvén eigenmode stability in JET internal transport barrier afterglow experiments. en. *Nuclear Fusion* **62**, 106001. ISSN: 0029-5515, 1741-4326. doi:[10.1088/1741-4326/ac84ee](https://doi.org/10.1088/1741-4326/ac84ee) (Oct. 2022).
39. Meijering, E. *et al.* Design and validation of a tool for neurite tracing and analysis in fluorescence microscopy images. en. *Cytometry Part A* **58A**, 167–176. ISSN: 1552-4922, 1552-4930. doi:[10.1002/cyto.a.20022](https://doi.org/10.1002/cyto.a.20022) (Apr. 2004).